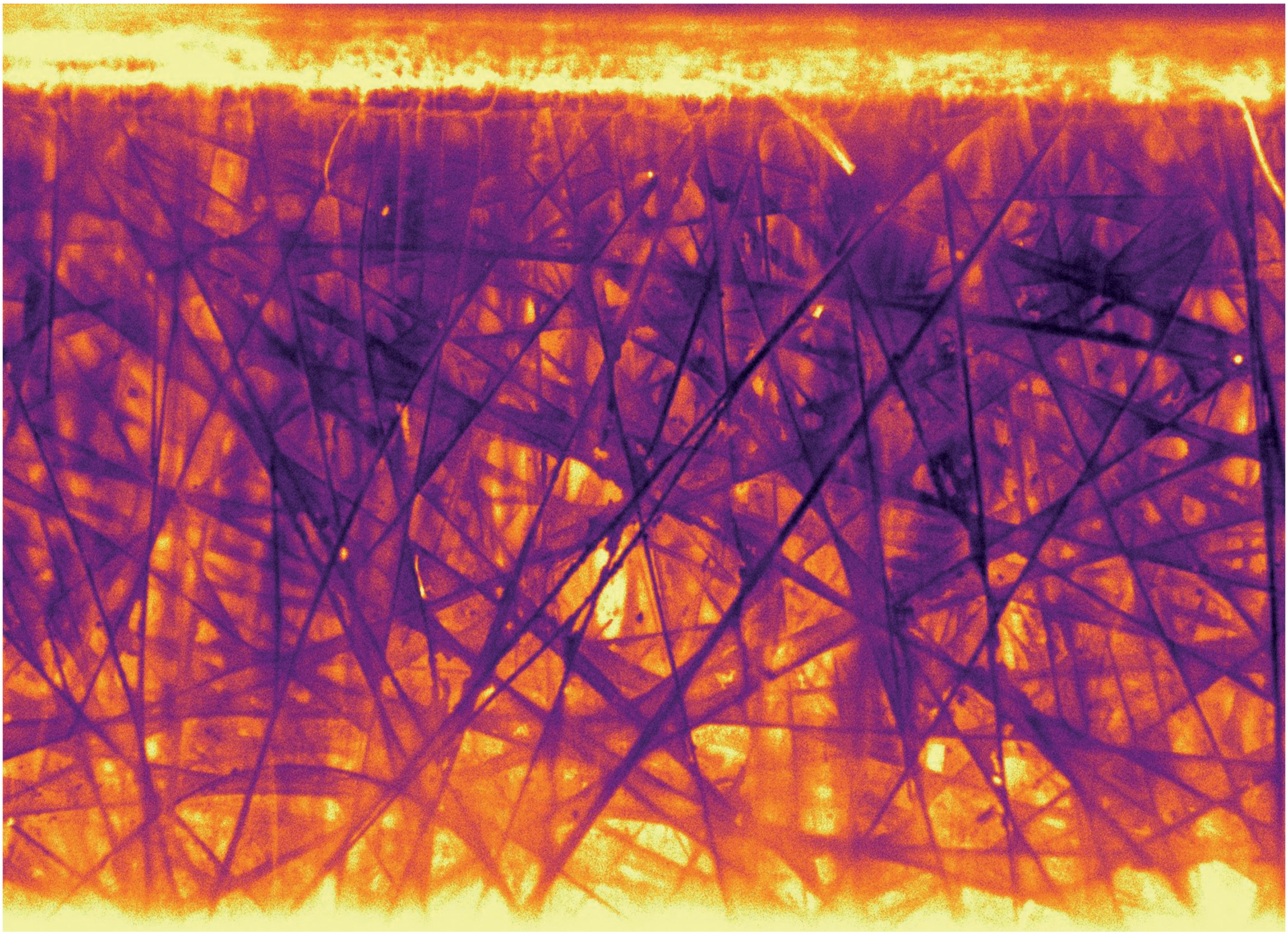

Showcasing research from Professor Michael J. Aziz's laboratory, Harvard John A. Paulson School of Engineering and Applied Sciences, Harvard University, Cambridge, Massachusetts, USA.

Quantitative local state of charge mapping by *operando* electrochemical fluorescence microscopy in porous electrodes

This image offers a peek inside an operating porous electrode, where electrolyte flows from top to bottom, and the redox-active organic species light up as they are charged along fibres. By coupling confocal fluorescence microscopy with *in situ* electrochemistry and rigorously calibrating the brightness, the state of charge and multi-species concentration fields are mapped with micron-scale resolution at video frame rates. This technique provides insights into the transport and chemical mechanisms in electrochemical flow devices.

As featured in:

See Shmuel M. Rubinstein, Michael J. Aziz *et al.*, *Energy Adv.*, 2024, **3**, 2468.

ROYAL SOCIETY OF CHEMISTRY

rsc.li/energy-advances

Energy
Advances

PAPER

View Article Online
View Journal | View Issue

Check for updates

Cite this: *Energy Adv.*, 2024, 3, 2468

Quantitative local state of charge mapping by *operando* electrochemical fluorescence microscopy in porous electrodes†

Anton M. Graf, ‡[a] Thomas Cochard, ‡[a] Kiana Amini, §[a] Michael S. Emanuel, [a] Shmuel M. Rubinstein *[b] and Michael J. Aziz *[a]

We introduce *operando* quantitative electrochemical fluorescence state of charge mapping (QEFSM), a non-invasive technique to study operating electrochemical systems along with a new design of optically transparent microfluidic redox flow cells compatible with the most demanding optical requirements. QEFSM allows quantitative mappings of the concentration of a particular oxidation state of a redox-active species within a porous electrode during its operation. In this study, we used confocal microscopy to map the fluorescence signal of the reduced form of 2,7-anthraquinone disulfonate (AQDS) in a set of multistep-chronoamperometry experiments. Calibrating these images and incorporating an analytical model of quinhydrone heterodimer formation with no free parameters, and accounting for the emission of each species involved, we determined the local molecular concentration and the state of charge (SOC) fields within a commercial porous electrode during operation. With this method, electrochemical conversion and species advection, reaction and diffusion can be monitored at heretofore unprecedented transverse and axial resolution (1 μm and 25 μm, respectively) at frame rates of 0.5 Hz, opening new routes to understanding local electrochemical processes in porous electrodes. We observed pore-scale SOC inhomogeneities appearing when the fraction of electroactive species converted in a single pass through the electrode becomes large.

Received 6th June 2024,
Accepted 27th August 2024

DOI: 10.1039/d4ya00362d

rsc.li/energy-advances

1. Introduction

To respond to the growing concerns over environmental consequences of the consumption of fossil fuels, our economy needs to rapidly undergo a transition to sustainable energy sources and technologies. Electrochemical devices and related systems are playing an increasing part in this energy transition. Electrochemical flow cells operate, for example, in redox flow batteries, fuel cells, electrolyzers and desalinators. Most such systems employ high surface area porous electrodes as the central neighborhood for electrochemical conversion, specifically to facilitate mass transport and increase reaction rates in 3D architectures.

Whereas considerable amounts of research have been conducted on macroscopic reaction-flow properties[1–3] and the microscopic properties such as surface functionalization and nano pores,[4–6] more work is required to understand the mesoscopic length scales in between, *e.g.* the concentrations, transport, and conversion of chemical species at scales from fibers to microstructures, which could make electrochemical flow devices more viable. Conventional electrochemical techniques, such as voltammetry, typically lack spatial resolution.[7] Voltage probes provide only sparse sample sets and are often invasive. Although, from voltage probes, losses can be attributed to processes occurring within porous electrodes,[8] the understanding of how these losses depend on the electrode microstructure, *i.e.* pore size or fiber diameter and their respective distributions and orientations, is still missing. Other *in situ* analytical methods, *e.g.* UV/Vis spectrophotometry,[9] nuclear magnetic resonance spectroscopy (NMR),[10,11] electron paramagnetic resonance spectroscopy (EPR),[12] or X-ray imaging[13,14] are under ongoing development but have not yet yielded data spatially resolved inside porous electrodes over mesoscopic length-scales.

A promising technique to overcome the current limitations and gain further insight into geometric effects of electrochemical conversion inside porous electrodes is offered by coupling *in situ* fluorescence microscopy with electrochemical monitoring. A variety of studies from the last decades utilized fluorescence microscopy coupled to electrochemistry[15] have been performed mainly to study electrochemical processes on planar electrodes in 2D,[16–20] defects[21,22] or for application in biomolecules.[23–28]

---

[a] *Harvard John A. Paulson School of Engineering and Applied Sciences, 29 Oxford St., Cambridge, MA02138, USA. E-mail: maziz@harvard.edu*

[b] *Racah Institute of Physics, The Hebrew University of Jerusalem, Jerusalem, Israel*

† Electronic supplementary information (ESI) available. See DOI: **https://doi.org/10.1039/d4ya00362d**

‡ These authors contributed equally to this work.

§ Present address: Department of Materials Engineering, University of British Columbia, Vancouver, BC, Canada V6T 1Z4.

Recently, the remarkable ability of confocal microscopes to quantify optical information from three spatial dimensions has been harnessed in electrochemical reactions. This advancement has enhanced the interpretation of variations in the adsorption patterns of organic agents, informed by surface morphology, and enabled the quantification of pH gradients in proximity to the electrode surface.[21,29,30]

Electrochemical reaction layers and microscopic heterogeneities on microelectrodes have been imaged in static electrochemical devices with a confocal fluorescence microscope.[31] Confocal fluorescence microscopy has also been used to map the local pH in the electrolyte near an operating gas diffusion electrode during electrochemical CO_2 reduction showcasing the effect of the micro-scale morphology on mass transport and hence the local electrochemical performance.[32,33]

Recently, 2D widefield fluorescence microscopy revealed substantial heterogeneities in the state of charge and electrolyte velocity field within commercial electrodes operating inside a flow cell.[34] The scale of these heterogeneities exceeded the characteristic pore size ($\sim$50 μm) by more than an order of magnitude, reaching length scales relevant to commercial flow batteries. This work called into question the validity of assuming a homogeneous Darcy-like flow and the use of Newman's porous electrode model in practical electrochemical devices at these scales.[35] The real-time investigation of electrochemical conversion was performed with 2,7-anthraquinone disulfonate (AQDS) and its corresponding hydroquinone, H_2AQDS, which results from a two-electron, two proton reduction and is accompanied by a significant change in its fluorescence signal.

The study of anthraquinone derivatives in flow batteries is also of great interest due to their synthetically controllable properties,[36–38] potential low cost,[39–41] earth-abundant building blocks and chemically mild operation.[42] Their realized lab-scale power densities, however, remain below those of vanadium flow batteries[43] and, in some cases, their internal resistance has been shown to be due, in large part, to the losses within the porous electrode imbibed with flowing aqueous organic electrolyte.[8] Such power losses are inherent obstacles in most electrochemical flow devices, underscoring the demand for the development of novel techniques to comprehend these losses across diverse length scales through accurate quantification of electrochemical conversion and local transport coefficients. Given that many organic-based, redox-active systems are optically active, they are amenable to analysis using *operando* confocal microscopy. Achieving spatial resolution in the quantification of electrochemical conversion provides a valuable opportunity to gain deeper insight into the nature and extent of these power losses.

Here, we introduce a non-invasive *operando* technique, namely quantitative electrochemical fluorescence state of charge mapping (QEFSM), to precisely quantify electrochemical conversion of redox active molecules at the single-digit micron scale and over time within electrochemical flow systems.

We transcended previous techniques by employing confocal fluorescence microscopy inside an operating porous electrode during the reduction of AQDS to quantify and map the local state of charge (SOC). This entails quantitatively differentiating the signal contributions originating from the various molecular species present. The incorporation of a confocal microscope enhances previous studies by providing depth-focused imaging which, in turn, enables accurate measurement of fluorescence intensity within a specified volume; this is crucial in relating the local species concentrations to spatial features of the electrode. Along with the technique we present a new microfluidic flow cell compatible with the optical requirements of the confocal microscope. Except for the electrode, current collector and the membrane, the flow cell is fully transparent, enabling excellent optical access to the pore space. The high porosity of the electrode allows access to the volume inside except for the regions where light is blocked by electrode fibers. Shadows and artifacts due to opaque fibers were removed throughout calibration and post-processing of the images. The SOC is evaluated locally at these optically accessible positions inside the porous electrode.

We further demonstrate that the dimerization of one AQDS molecule with one H_2AQDS molecule to form quinhydrone (QH) affects the fluorescence intensity. While this can be quantified by our visualization technique, it cannot be discerned with the electrochemical measurements of the cell alone. The SOC is estimated by iteratively calibrating observed image intensities using a model with no free parameters, which includes a reversible 1 : 1 (AQDS : H_2AQDS) binding dimer, which is further supported by prior experimental work.[9] Whereas the heterodimer can influence the intensity, it should not impact the detected current or the accessible storage capacity in AQDS solutions at concentrations used in this study, as over 90% of theoretical capacity has been demonstrated in 1 M solutions.[44] By employing a calibration technique that incorporates dimer formation and enables the separation of distinct signal contributions of AQDS, H_2AQDS and dimer, we develop a consistent quantification of fluorescence, the local optical environment, and all three concentrations.

Under the operating conditions considered in this study, the spatially averaged and dimer-corrected image intensity monotonically increases with (and is approximately linear in) the total current. The resulting local SOC maps offer a robust tool for quantifying and evaluating local variations in electrochemical conversion and transport within complex porous electrodes. Our findings contrast with the simple assumption of a constant gradient along the macroscopic flow direction. Such insights are valuable for future research evaluating the domain of suitability of such assumptions. We expect QEFSM to not only improve the understanding of electrochemical conversion and transport of other redox-active species, but also to greatly aid in the understanding of porous electrodes and their microstructures as active materials in electrochemical devices.

2. Working principles and experimental setup of *operando* QEFSM

2.1 Design and fabrication of transparent microfluidic flow cells

Our microfluidic electrochemical cell design, shown in Fig. 1, enables the synchronous study of electrochemical reaction with a conventional potentiostat and the spatially resolved fluorescence intensity. The non-invasive *operando* study of optically active electrolytes *via* confocal fluorescence microscopy necessitates the design of an electrochemical cell that is compatible with optical imaging. The cell we introduce in this study is optically transparent and permits optical access to the entire electrode, as shown in Fig. 1(A) and (B). Two half cells are fabricated from PDMS (Polydimethylsiloxane) with acrylic backing. To visualize the inside of the electrode, a relatively long working distance (<11 mm), high-resolution microscope objective used.

The flow cell is designed for small working electrodes (3 × 6 mm^2) allowing an effective study of the entire electrode under high magnification (10×). A single flow channel transports the electrolyte into, through, and out of the electrochemical cell, as shown in Fig. 1(A) and (B). The cell was constructed of two half cells, an anode and a cathode, each embedded in a thin, optically transparent PDMS slab (see ESI,† Section 1 for details). The anode side includes 1 × 1 mm^2 channels in a serpentine geometry supplying the Pt-coated carbon electrode with humidified hydrogen gas. This electrode is much larger (10 × 20 mm^2) than the one on the cathode side, ensuring that the cathodic reaction on the working electrode remains rate limiting. Hydrogen flow was controlled *via* a manual pressure adjusted to ensure that a bubble emerged approximately every two seconds from a plastic tube at the cell exit, which was immersed in water. Hydrogen underwent oxidation on a Pt-coated carbon electrode, with resulting protons crossing the membrane for net charge neutrality.

The cathode or working electrode side, the PDMS contained a 1.0 × 0.5 mm^2 flow channel that supplied the porous electrode with electrolyte as shown in Fig. 1(A). The aqueous electrolyte on the cathode side consisted of 10, 20, 30 and 40 mM of AQDS in 1 M sulfuric acid. The acid served as a supporting electrolyte whose protons were involved in the proton-coupled electron transfer in the AQDS reduction reaction (see Section 2.2). A syringe pump was used to drive the electrolyte flow at constant flow rate. The superficial flow velocity, defined as the ratio of the volumetric flow rate Q to the nominal cross-sectional area A of the electrode by the formula $u_s = Q/A$ and without correcting for the porosity or the compression of the electrode, was 2.3 mm s^{-1}. A Reynolds number of ∼14 indicates laminar flow, suggesting steady-state conditions with no expected time-dependent variations in the flow. A commercial AvCarb MGL 190 carbon paper of nominal thickness 190 μm was used as the working electrode. This electrode has a disordered fiber microstructure held together by a binder material, as shown in Fig. 1(C). The electrode was baked for 24 h at 400 °C to increase its hydrophilicity.[2] The proton-conducting separator (Nafion 212) was soaked in 1 M sulfuric acid prior to the experiments. The PDMS half cells, electrodes, and membrane were compressed by transparent acrylic endplates and screws, providing an excellent seal that obviates the use of gaskets, as shown in Fig. 1(B).

Experimentally, we showcased the capabilities of QEFSM utilizing the AQDS/H$_2$AQDS redox system as the optically active electrolyte. In all experiments, the electrochemical cell was placed on top of an inverted spinning disk confocal microscope with a 10 × 0.3 NA air objective and 50 μm pinhole size. Transverse (x–y) and axial (z) resolution are 1 μm and 25 μm, respectively. The short depth of field is one of the major advantages of QEFSM compared to previous studies that used fluorescence microscopy as it allows us to determine a precise volume for each frame. In this study, images of fluorescence intensity were captured simultaneously over a 1.2 × 1.2 mm^2 field of view close to the center of the working electrode. The transparent PDMS casing allowed the study of an arbitrary position inside the electrode as well as an arbitrary depth from the surface toward the opaque membrane as the focal plane is adjusted. For orientation inside the electrode, we located the interface between PDMS and electrolyte and moved toward the membrane to a depth of 50 μm. The electrochemistry was controlled and measured by a potentiostat (see ESI,† 1 and 2). We acquired dynamical fluorescence image stacks at 2 seconds exposure time spanning over pre-defined volumes within the porous electrode while varying the applied potential. While it is

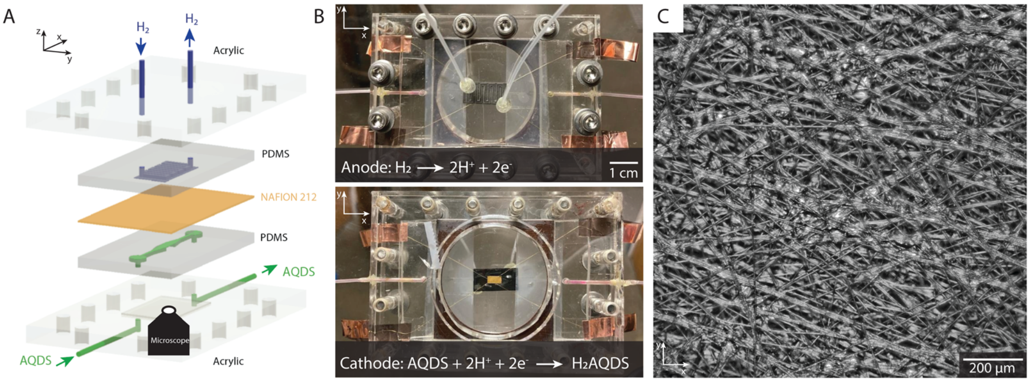

Fig. 1 Microfluidic flow cell compatible with electrochemistry and confocal microscopy. (A) Exploded view of the individual components with Cartesian coordinate nomenclature identified. (B) Images of the assembled cell from above (top) and below (bottom). The working electrode (3 × 6 mm^2) is visible in the center of the bottom image. For the bottom picture a working electrode made of gold was used to ensure visibility against the counter electrode in the background. (C) Widefield optical microscopy image of a section of a commercial AvCarb MGL 190 porous carbon paper electrode inside the electrochemical cell.

possible to significantly reduce the exposure time, a deliberate choice was made to employ a longer exposure time in this study in order to enhance signal resolution and generate high-quality maps.

2.2 Properties of the optically active AQDS electrolyte

The redox-active species AQDS in its various oxidation states, shown in Fig. 2(A), is a suitable molecular system to study electrochemical conversion inside porous electrodes.[9,34] We distinguish between the oxidized and reduced species (AQDS and H_2AQDS, respectively) by imaging at an emission band dominated by H_2AQDS as shown in Fig. 2(B). Calibration was performed with samples of known concentrations of AQDS, the stable form in equilibrium with air, and then reducing it by controlled amounts to obtain electrolyte emissions spectra at various proportions between the species.

We obtained the emission spectra of the 40 mM AQDS electrolyte at multiple SOCs using a plate reader after different amounts of electrochemical reduction aiding the quantitative correlation between state of charge (SOC) and fluorescence intensity, as shown in Fig. 2(B) and (C). Electrolytes were prepared from a pure and degassed 40 mM AQDS stock solution. The electrolytes were charged in a conventional bench scale flow battery *vs.* V^{3+}/V^{4+} across a Nafion 212 membrane to obtain a series of different SOCs (0, 30, 40, 50, 60, 70, 80 and 90%). A 405 nm wavelength laser was used to excite the optically active molecules in the system. H_2AQDS exhibits an absorption peak proportional to its concentration.[9] The emission spectra of the AQDS/H_2AQDS system at various SOC, shown in Fig. 2(B), showed a broad peak whose height increases with SOC. This broad emission peak was captured by the microscope's imaging sensor with a green bandpass filter with a range between 500 and 525 nm and integrated in the microscopy studies described below. Contrary to initial expectations,[34] the integrated raw fluorescence intensity measured by the microscope as a function of SOC shows a nonlinear increase, as illustrated in Fig. 2(C).

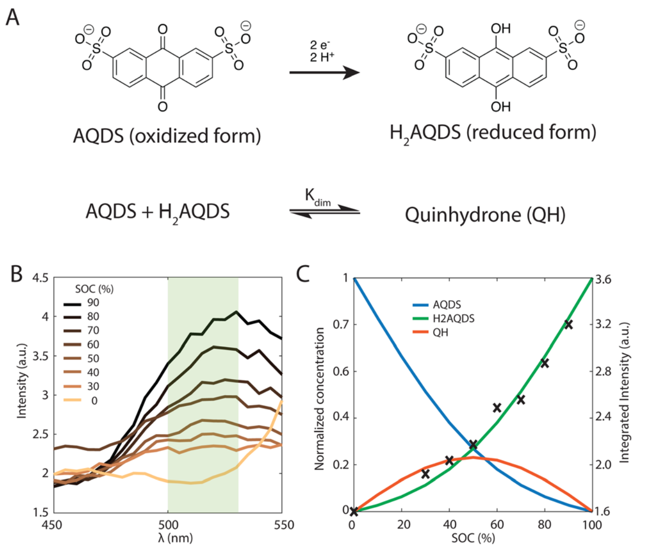

Fig. 2 Fluorescence Properties of the AQDS and H_2AQDS redox couple. (A) Reduction scheme of AQDS to H_2AQDS *via* proton-coupled electron transfer (top). Stoichiometric equation for the heterodimerization of AQDS and H_2AQDS to quinhydrone (QH) (bottom). (B) Emission spectra of 40 mM AQDS solutions as a function of emission wavelength λ at different SOCs obtained at an excitation wavelength of 405 nm. The shaded rectangle indicates the range accepted by the green bandpass filter of our confocal microscope. (C) Raw intensities integrated over the shaded region in (B) *vs.* SOC (right *y*-axis). The solid lines are the theoretical normalized concentrations of H_2AQDS (green), AQDS (blue) and QH dimer (red) predicted by the 1 : 1 (AQDS : H_2AQDS) binding dimer model for initial concentrations of 40 mM (left *y*-axis).

If the only contribution to the SOC were from H_2AQDS, we would expect the fluorescence intensity to be linearly increasing with SOC. Thus, the observed nonlinear response indicates that competitive photophysical processes due to chemical electrolyte interactions, such as self-absorption, fluorescence quenching, molecular decomposition or electrolyte interactions, should be considered. We eliminated electrolyte decomposition as an explanation because the capacity fade rate of the AQDS/H_2AQDS systems lies around 0.08%/day and we were not reusing any of the electrolyte from day to day.[45] Although we were not able to exclude other mechanisms with certainty, the dynamical formation of quinhydrone dimers (QH), as shown in Fig. 2(A) provides a logical and quantitative explanation of the nonlinearity measured in fluorescence intensity. In previous studies[9] measuring the absorption spectra for these species, it was found that when both are present, one molecule of AQDS and one molecule of H_2AQDS can reversibly bind to form a quinhydrone heterodimer (QH) as shown in Fig. 2(A). A value of 80 M^{-1} was deduced for the equilibrium constant K_{dim} of the association reaction.

We propose that the dimer species does not contribute significantly to the detected fluorescence and therefore reduces the measured intensity by lowering the concentration of H_2AQDS, the only significantly fluorescent species in the mixture. Based on this hypothesis we are able to construct an effective 1 : 1 (AQDS : H_2AQDS) binding dimer model that quantitatively corrects the SOC by the amount of reduced electrolyte that became invisible due to dynamic dimer incorporation (see ESI,† Section 4). During the electrochemical reduction of AQDS, some of the charge resides in the H_2AQDS and some in the dimer. Thus, the dimer should be regarded as another reduced species. If [QH] represents the concentration of the QH, then the state of charge (SOC) may be defined as

$$\mathrm{SOC} = \frac{[\mathrm{H_2AQDS}] + [\mathrm{QH}]}{[\mathrm{AQDS}] + [\mathrm{H_2AQDS}] + 2[\mathrm{QH}]}, \tag{2.1}$$

where, in the absence of decomposition, the denominator is invariant in the chemical and electrochemical processes involved. A SOC of 0% corresponds to a fully oxidized solution of pure AQDS and a SOC of 100% corresponds to a fully reduced solution of pure H_2AQDS. At those two extremes no dimer is present. This provides us with a system of equations that can be solved for different initial concentrations of AQDS, $[\mathrm{AQDS}]_0$, to predict the expected concentration of AQDS, H_2AQDS and QH as functions of SOC, as shown in ESI,† 4. Assuming the initial electrolyte is always in its fully oxidized form, having equilibrated with air, the denominator of eqn (2.1) equals $[\mathrm{AQDS}]_0$.

The results shown in Fig. 2(C) demonstrate that overlaying the experimental intensity data with the theoretical normalized H_2AQDS concentrations predicted from the dimer model reproduces this nonlinear increase closely. Hence, we concluded that the fluorescence intensity is proportional to [H_2AQDS] and [QH] does not significantly contribute to the total intensity of the redox-system. Whereas the dimer formation lowers the measured fluorescence intensity, it participates in the current extracted. For the given dimerization mechanism, the ratio of dimer formed to $[\text{AQDS}]_0$ increases as $[\text{AQDS}]_0$ grows, as shown for all experimentally relevant cases in ESI,† 4. Because of the thermodynamic equilibrium of the equation shown in Fig. 2(A), the dimer fraction as a function of the SOC has the functional form of an inverted parabola. The dimer concentration initially grows and is the largest at 50% SOC when the concentrations of AQDS and H_2AQDS are equal, beyond which it decreases to 0 M at 100% SOC, as shown in Fig. 2(C). In experimental data with sufficiently high $[\text{AQDS}]_0$, such as the presented case of 40 mM, the concentration of QH can surpass that of H_2AQDS indicating a prevalence of charged species in the form of dimer rather than H_2AQDS, which affects the fluorescence intensity significantly. As a consequence, the intensity calibration *vs.* SOC, which must account for the amount of dimer that contributes to the SOC but only weakly to the emitted intensity, varies with $[\text{AQDS}]_0$. This calibration qualifies the AQDS/H_2AQDS system as a suitable system to exactly quantify SOC maps through QEFSM.

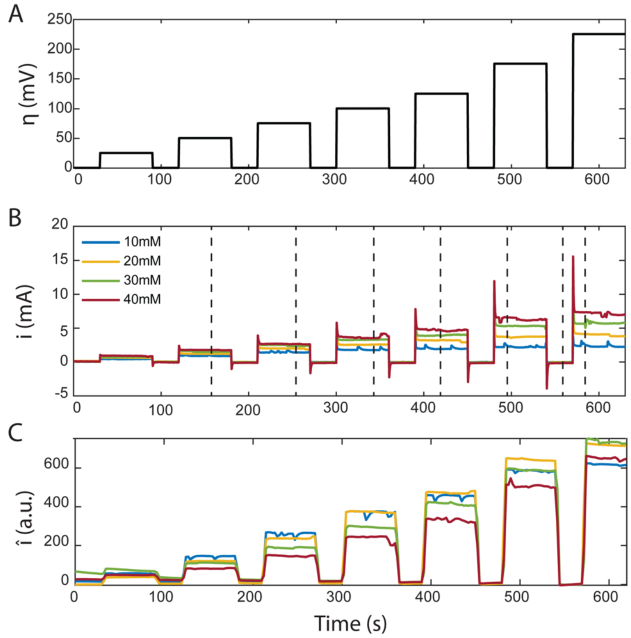

Fig. 3 Characteristic plots from MSC of AQDS at different concentrations flowing through an AvCarb MGL 190 porous carbon electrode paper. (A) shows the time dependence of the applied stepped cell overpotentials (25, 50, 75, 100, 125, 175 and 225 mV). (B) Shows the measured reduction current corresponding to the overpotentials above for different reactant concentrations. (C) Shows the mean fluorescence intensity detected in a $1.2 \times 1.2\ \text{mm}^2$ frame inside the confocal microscope over the same period. All average intensity values were background corrected.

3. Results and discussion

3.1 Multi-step chronoamperometry studies with *operando* confocal fluorescence microscopy

With electrolyte flowing steadily, we imposed stepped cell voltages and measured the resulting current according to a multi-step chronoamperometry (MSC) protocol (*vide infra*). Simultaneously, we measured the varying fluorescence intensity field with the optical apparatus of a confocal fluorescence microscope, from which we obtained the concentration fields. In a flow cell, the temporal change of the concentration field C_j of species j has contributions from advection A_j, diffusion D_j, and electromigration ε_j in addition to the electrochemical source S_j, which is proportional to the faradaic component of the electrical current.

$$\frac{\partial C_j}{\partial t} = A_j + D_j + \varepsilon_j + S_j. \tag{3.1}$$

In steady-state, the concentration of a species converted in a specified volume element is determined by the balance between the source term, which depends on the overvoltage through the current, and the removal from that volume element *via* the net combined effects of advection, diffusion, and electromigration, which scale with concentration, as further described in ESI,† Section 5.

In the MSC experiment each potential step was held constant for 60 seconds to obtain a stable steady-state-current as shown in Fig. 3(A). We measured the current i as we increased the overpotential η successively from 25 to 225 mV in increments of 25 or 50 mV, which increased the electrochemical driving force that governs the reaction rate, as shown in Fig. 3(B). To prevent hydrogen evolution, we refrained from using higher overpotentials. Before each change in the step-potential we set the cell potential to open-circuit voltage (OCV), the potential at which no current is passing, for 30 seconds maintaining the flow of degassed electrolyte.

The current spike following each change in cell potential was caused by capacitive current. This event was followed by a steady-state faradaic current that was monitored for the remainder of each potential step. The faradaic current is governed by the reaction rate at the electrode. Despite maintaining a steady voltage, we observed small fluctuations in the current over time, which are captured in Fig. 3(B). These fluctuations can be caused by the competing reaction of hydrogen evolution from the electrolyte. For increasing values of $[\text{AQDS}]_0$, higher steady-state currents were observed because greater reactant concentrations were available to become reduced in each time interval.

The confocal microscope simultaneously produced raw intensity maps I_{raw} for each image. To investigate the relationship between the current and the fluorescence intensity we first quantified the average fluorescence of each image (sampling time interval Δt = 2.5 s). Our initial analysis entailed averaging I_{raw}, across the entire image, yielding $\bar{I}_{\text{raw}}$. For better visualization in Fig. 3(C) we subtracted the background fluorescence image captured at OCV prior to the spatial averaging of the intensity in each individual frame. The resulting mean background-corrected fluorescence intensity $\hat{I}$ follows the current response closely for all potentials applied. Interestingly, the small variations in current were relatively well captured by the average fluorescence intensity $\hat{I}$. Any negative intensity fluctuation was correlated to a positive current fluctuation. This supports the hypothesis that hydrogen evolution competes with AQDS reduction. Small hydrogen bubbles, nucleating in pockets of presumably inhibited flow, transiently cross the image, momentarily decreasing average intensity, despite contributing to the overall detected current through water reduction to hydrogen. This behavior, depicted in Fig. 3 comparing (B) and (C), exhibits minor variations relative to their average values at each chronoamperometry step.

The current, sampled in steady state after each potential step, indicated by the dashed lines in Fig. 3(B) and reported in the polarization curves in Fig. 4(A), increased linearly with overpotential for the first ∼100 mV. Superlinear behavior, apparent at higher potentials, is indicative of mass transport limitations. The overall utilization of electrolyte, u, defined as the faradaic charge passed to the electrolyte on a single pass through the device divided by its theoretical maximum value set by the charge capacity of the molecules, decreased for increasing $[\mathrm{AQDS}]_0$, as shown in Fig. 4(B). When the electrolyte at the inlet is fully oxidized, as it always is in work reported here, the utilization can be expressed analytically in terms of the total current J, the volumetric flow rate Q, the concentration of species available for reduction in the entering electrolyte given by $[\mathrm{AQDS}]_0$, Faraday's constant F and the number of transferred charges per molecule n:

$$u = \frac{J}{Q \cdot [\mathrm{AQDS}]_0 \cdot F \cdot n} \tag{3.2}$$

Despite the higher currents at increasing concentrations of electrolyte under the same applied potentials, Fig. 4(B) shows the utilization of electrolyte decreasing with increasing $[\mathrm{AQDS}]_0$. Furthermore, we observed that for $[\mathrm{AQDS}]_0$ of 10 mM, high utilizations of up to 88% were achieved while the utilization of electrolytes with higher concentrations are lower and closer to each other for the same applied potentials. We posited that the fluorescence intensity of every molecular species under consideration is linearly proportional to its concentration within the examined regime. Consequently, the aggregate raw intensity I_{raw} is the cumulative sum of these individual contributions depending on the concentrations at each specified SOC, with each species possessing a distinct emission coefficient. A schematic representation of the various fluorescence contributions is provided in ESI,† 6. As depicted in Fig. 4(C), the uncorrected mean intensities $\bar{I}_{\mathrm{raw}}$ (extracted at the same sampling times indicated by the dashed lines in Fig. 3(B)) associated with their varying initial concentrations, $[\mathrm{AQDS}]_0$, do not conform to a singular linear calibration curve. Because of dynamic formation of dimer, which has notably reduced fluorescence, the total intensities do not directly correlate with the amount of charge transferred. It is observed that discrepancies, or nonlinear effects, amplify with increasing $[\mathrm{AQDS}]_0$, which is again supported by the dimer model with fixed equilibrium constant K_{dim}. At OCV, in the absence of $\mathrm{H_2AQDS}$ and QH, the observed increase of $\bar{I}_{\mathrm{raw}}$ corresponding to elevated $[\mathrm{AQDS}]_0$ reveals the intrinsic fluorescence of AQDS, alongside an assumed constant background. With a correct calibration, accounting for both the intrinsic fluorescence of AQDS, the dynamic dimer formation, and the background, the curves should overlay one another, irrespective of the initial concentration $[\mathrm{AQDS}]_0$. As a possible solution, we introduce a calibration tailored for each location (pixel). This calibration is predicated on a numerical fit, taking into account the emission profile of each molecular species relative to its concentration, all as functions of SOC. The detailed calibration procedure is presented in the subsequent section.

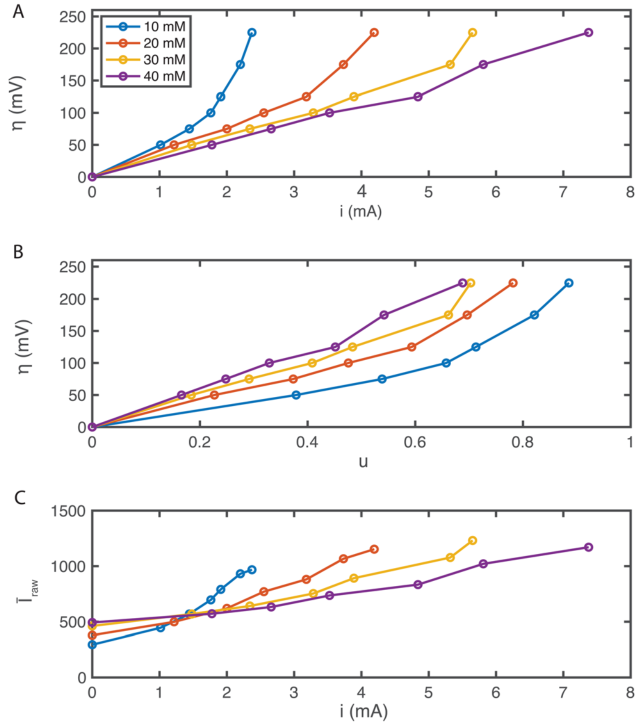

Fig. 4 Characteristic plots from MSC experiments. (A) Polarization plot as a result of the MSC experiment for $[\mathrm{AQDS}]_0$ values indicated. (B) Applied overpotentials as function of the electrolyte utilization u. (C) Mean raw fluorescence intensity $\bar{I}_{\mathrm{raw}}$ averaged over the entire confocal microscope image as a function of the current i.

3.2 Local SOC and concentration mapping

3.2.1 Calibration. Assuming a linear model of light emission P by each chemical species present, the theoretical light intensity mapped to a single pixel of the imaging sensor is given by:

$$P_{ri} = \alpha[\mathrm{AQDS}]_{ri} + \beta[\mathrm{H_2AQDS}]_{ri} + \gamma[\mathrm{QH}]_{ri} + \delta \tag{3.3}$$

where α, β, and γ are the brightness coefficients of the three electroactive species, and δ is the brightness of the supporting electrolyte. The subscripts denote reaction condition r, specified by overpotential η and initial AQDS concentration $[\mathrm{AQDS}]_0$, and pixel i. In practice we need to consider optical aberrations, *e.g.* due to sample irregularities, out-of-focus light, reflections, and background noise. Thus, we further propose a linear model of observed image intensity I which is proportional to light production,

$$I_{ri} = F_i P_{ri} \tag{3.4}$$

where F_i is the optical factor at pixel i and is higher in regions that are less obstructed by fibers. To account for the finite axial resolution, we interpret the results from each pixel as representing the average SOC within an electrolyte column. The depth of each column is equal to the portion of the slab's thickness contributing to the image, excluding the volume blocked by a fiber at the far end of the column. Pixels for which this column is deeper have higher optical factors. Given the chemical equilibrium of dimer formation, we can uniquely solve for the concentration of all three species with the only free parameter for each pixel being the fraction of reduced species Y, defined by

$$Y_{ri} = \frac{[\mathrm{H_2AQDS}]_{ri}}{[\mathrm{AQDS}]_{ri}+[\mathrm{H_2AQDS}]_{ri}+2[\mathrm{QH}]_{ri}} = \frac{[\mathrm{H_2AQDS}]_{ri}}{[\mathrm{AQDS}]_{0r}}. \tag{3.5}$$

Our general approach, elaborated in detail in ESI,† 6, is to map the state of charge by jointly estimating the brightness coefficients α, β, γ, δ the optical factors F_i; and the reduced species fraction Y_{ri}, from which we can directly calculate the SOC.

3.2.2 Operando SOC mapping.

As a result, the intensity of each pixel is mapped into an SOC value, as shown in Fig. 5. The potential-concentration chart Fig. 5(A) shows the 2D operando SOC maps for 10, 20, 30 and 40 mM electrolytes from the top to the bottom. From the left to the right increasing overpotentials of 50, 100 and 175 mV are displayed with the insets indicating utilization derived from the steady-state current. The fiber structure of the electrode now appears as the white areas. With the increase in overpotential, leading to enhanced utilization, a corresponding rise in local SOC values is observed. Across the selected imaging region, higher utilizations consistently elevate

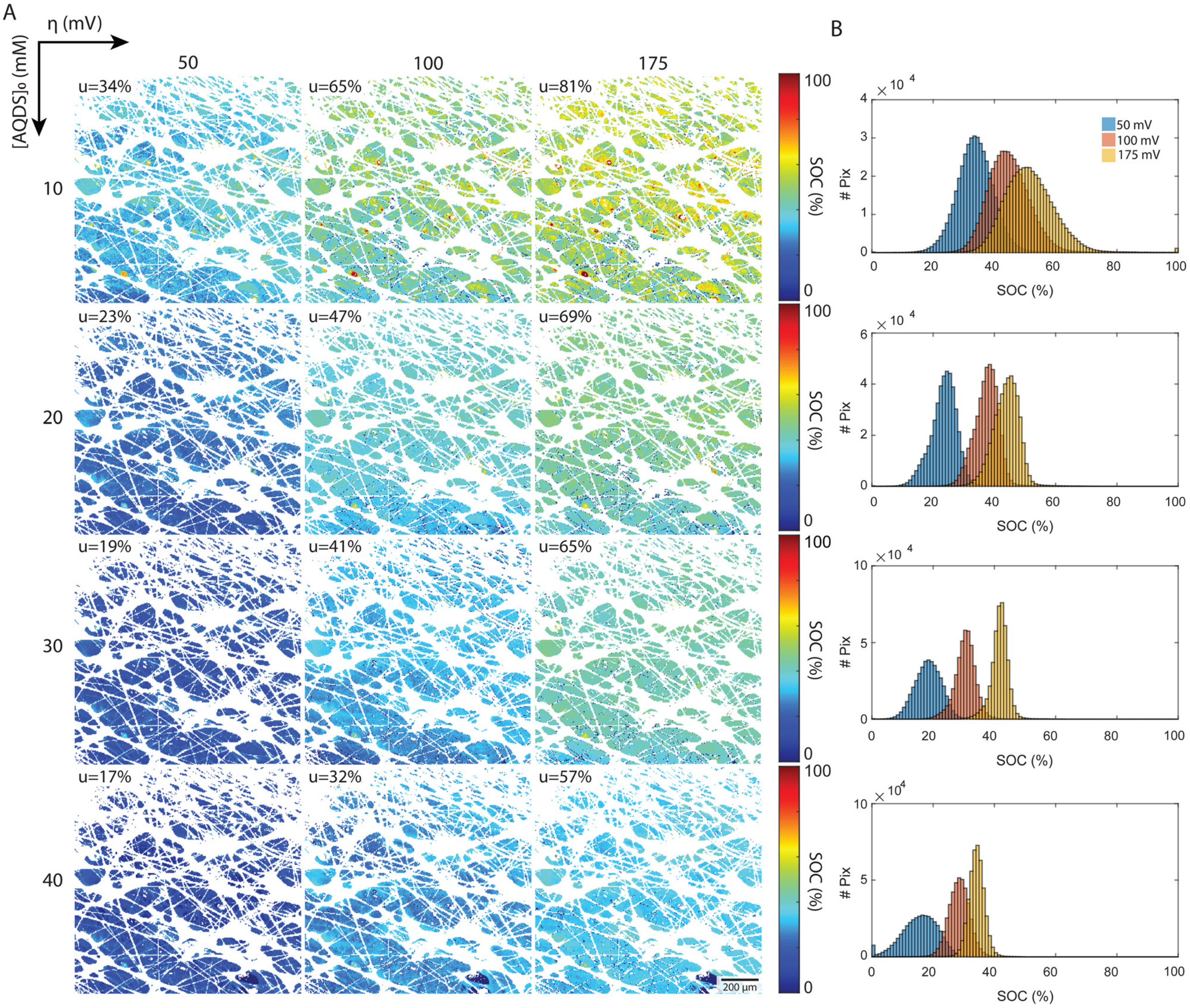

Fig. 5 Local SOC deduced from fluorescence intensity maps. (A) Chart of steady-state fluorescence maps under varying conditions. The applied overpotentials are increasing from left to right (50, 100, 175 mV). The initial concentrations of redox-active AQDS (10, 20, 30, 40 mM) are increasing from top to bottom. The color map indicates the H_2AQDS concentration as a fraction of the initial concentration. The white pixels correspond to fibers and hetero-phase impurities that are removed during image processing by converting them to NaN values. (B) Histograms of the concentration distribution over all pixels for each image where NaN values are removed. Each plot corresponds to the concentrations in the row to its left.

local SOC values, even near the center of the electrode, though not in a uniform manner. Thus, a shift in the mean SOC, $\bar{S}$, across the image cannot be solely attributed to a straightforward multiplicative effect on each pixel. Instead, specific regions where the SOC appears less sensitive to variations in overpotential can be identified. These areas have a lower contribution to the overall electrochemical conversion process, highlighting the opportunity for a better understanding of their mass transport characteristics in future studies.

The local SOC maps of the 1.2 × 1.2 mm^2 field reveal a field of increasing SOC, transitioning from the lower left to the upper right of each image. Given that the optical factor F_i corrects for spatial variations in emitted and detected light, we believe that this trend represents real physical processes and suggests that Darcy flow is an inadequate description of flow at these length scales. The 2D SOC maps at the highest utilization show pronounced local variation at length-scales from the fiber diameter to the characteristic pore size. These are the length scales where reactant depletion should be most severe. That this pattern is not apparent at lower utilizations might be related to the fact that we are working with integrated intensity through a slab of roughly 25 μm in the direction of the optical path. Large regions exhibiting uniform SOC may indicate low electrochemical conversion, suggesting the possibility of low electrode and flow path efficacy in the region.

A more detailed quantitative look is reported in the histograms, which depict the distribution of pixels by their SOC values. All experimental distributions resemble normal or skewed distributions, as shown in Fig. 5(B). In the low concentration experiments ($[\text{AQDS}]_0$ = 10 mM), the histograms exhibit broader distributions than in the other cases. For $[\text{AQDS}]_0$ = 30 and 40 mM, histograms show that the SOC distributions become narrower as overpotential and utilization increase. At these higher concentrations, the SOC histograms have a distinct peak, indicating a mostly uniform SOC across the entire image.

For comparison, in the simple picture with a constant gradient in SOC along x, the macroscopic flow direction, the expected SOC histograms result in rectangular distributions centered at $\bar{S}$ and a width given by $u\Delta x/L$, where Δx is the width of the image and L is the length of the entire electrode in x. For our setup with Δx = 1.2 mm and L = 6 mm, those rectangular distributions would have a width of $0.2u$ SOC values for each histogram (see ESI,† 6 for comparison). The histograms derived from the experiments are typically narrower than this. Intriguingly, for the specimen with the highest utilization, $[\text{AQDS}]_0$ = 10 mM, under conditions where mass-transport limitations become apparent (Fig. 4(A)), the width of the SOC distributions from experiment exceeds the width of the hypothetical rectangular distributions.

Remarkably, combined analysis of the experimental histograms and SOC maps reveals that under varying conditions, we can observe either heightened local heterogeneity or enhanced uniformity. While these deviations might average out across larger areas, they are significant at the scale of the displayed 1.2 × 1.2 mm image frame. Such nuances might impact mesoscopic transport in electrochemical flow devices operating under practical conditions. Because this particular experiment collected the fluorescence from only a limited depth range of the electrode – the focal plane is set at z = 50 μm within the 190 μm thick electrode, with the z = 190 μm coordinate denoting the interface of the electrode with the membrane – we cannot determine the average state of charge throughout the entire thickness. We expect more comprehensive investigations to provide further insight, guide model development and, ultimately, permit the design of higher-performance electrodes. These investigations might encompass imaging across the entire x–y plane of the electrode, and at varied z-depths, and to examine transient, in addition to steady-state, behavior. For an example of visualization of transient concentration field evolution, dynamical videos are shown in the ESI,† 7.

Utilizing the SOC maps, we can infer the concentration fields of other species involved in the electrochemical process, specifically AQDS, H_2AQDS, and QH. Fig. 6 illustrates the average concentrations of these species within the imaging frame as functions of the average SOC, $\bar{S}$. These plots reflect the close alignment with the average concentrations predicted by the dimer model discussed in Section 2.2 and ESI,† 3. This reaffirms the pronounced influence of dimer formation at elevated concentrations. Such influence introduces non-linearities in the concentration profiles which, in turn, have implications for the measured intensities, emphasizing the necessity for precise calibration.

The formation of dimers has previously been discussed as having a limiting impact on accessible capacity, even at low

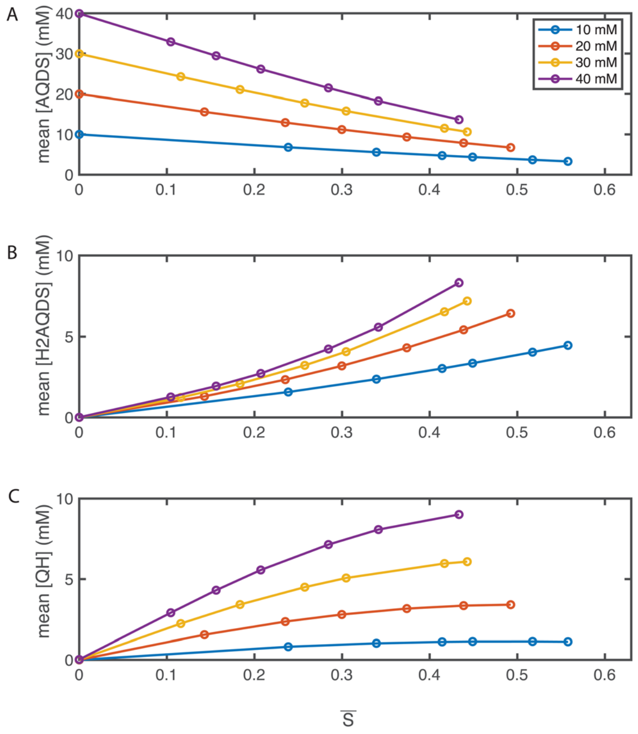

Fig. 6 Operando concentration profiles. Mean concentrations of (A) AQDS; (B) H_2AQDS; (C) QH as functions of the mean SOC $\bar{S}$ within in the field of view.

electrolyte concentrations.[46,47] This is in contradiction with other findings, where over 90% of theoretical capacity has been accessed in a flow battery utilizing 1 M AQDS concentration.[8] In the present study, we reached electrolyte utilizations of 70% or more at all concentrations, and 88% utilization at 10 mM despite dimer formation at concentrations shown in Fig. 6(C). As dimerization is concentration-dependent, QEFSM at higher concentrations of active material might reveal dimer effects on electrochemical behavior.

In this first demonstration of QEFSM, we show the potential this technique holds for mapping the concentrations of electrochemically active species within complex architectures, such as in electrochemical flow cell porous electrodes. This approach allows for in-depth examination of these systems across a range of operating conditions, offering valuable insights into intricate transport phenomena. Although not demonstrated here, by obtaining two-dimensional (2D) SOC maps at different depths within the porous electrode, we have the potential to reconstruct three-dimensional (3D) volumes encompassing local SOC and concentration fields.

As research in this domain becomes more rigorous, it will require more precise quantification, such as that provided by QEFSM, of local transport behavior and a deeper understanding of structure–function relationships from the pore-scale to the macro-scale. Such advancements are poised to enhance the design and performance of the forthcoming generation of electrochemical devices.

4. Conclusions

In this study, we have demonstrated a non-invasive *operando* technique for the precise mapping of concentration fields within a functioning porous electrode. By coupling electrochemistry and confocal microscopy inside the device we are able to derive spatially and temporally resolved SOC maps in well-defined volumes inside the electrode architecture. Transverse and axial resolution of 1 and 25 μm, respectively, were achieved.

We developed an optically transparent flow cell that facilitates the investigation of the entire electrode and is compatible with the confocal microscope hardware. The versatility of the setup makes it suitable for a wide range of porous architectures and optically active electrolytes. We demonstrated an effective image processing technique to address challenges associated with the presence of opaque components, including fibers at various z-heights and heterophase artifacts. Because the detected signal comprises distinct contributions from reactants, products, other interacting species, and background, we developed a calibration technique that enables quantification of concentration fields for all relevant molecular species within the system: the oxidized species [AQDS], the reduced species [H_2AQDS], and the dynamically formed heterodimer [QH]. Consideration of individual species concentration fields yields quantitative local SOC maps.

We have demonstrated that 2D mapping techniques offer a powerful method for characterizing local heterogeneity in concentration and SOC fields over mesoscopic areas inside of porous electrodes. This technique should permit experimental testing of multiphysics transport models from sub-pore scale to the scale of the field of view, which may be tiled to study larger areas. Within the limited 1.2 × 1.2 mm^2 field of view of these experiments, we observed the average gradient in the SOC field not parallel to the nominal flow direction, suggesting that Darcy flow is too simple a model for this length scale. We identified more uniform SOC fields at high concentrations and low utilization and broad SOC distributions for the lowest concentration with – particularly at the highest utilization – significant local heterogeneities at length scales from the fiber diameter to the characteristic pore size.

QEFSM is a valuable method to quantitively study porous electrodes as active materials during electrochemical transformations. It should facilitate the understanding of local voltage losses and the development of structure–function relationships for various electrode architectures. It may lead to electrochemical systems with improved performance and a new generation of electrode designs.

Author contributions

AMG, TC, KA, SMR and MJA designed and conceptualized the project. MJA and SMR supervised the project. TC and AMG developed cell prototypes. TC designed and fabricated the final version of the transparent PDMS electrochemical flow cell. AMG performed the operando confocal experiments and acquired the data. AMG and KA conducted *ex situ* and plate reader experiments and acquired the data. AMG, TC, MSE and KA developed and implemented the dimer model. TC performed initial image processing for SOC mapping. MSE developed the pixel-by-pixel calibration method and performed the final image processing. TC, MSE and AMG made the figures. AMG wrote the original draft of the manuscript. AMG, TC, KA, MSE, SMR and MJA revised the manuscript.

Data availability

Data for this article, including micrograph images and Python source code for data analysis, are available at qefsm at **https://doi.org/10.5281/zenodo.11505668**.

Conflicts of interest

There are no conflicts to declare.

Acknowledgements

This research was supported by U.S. Department of Energy, Office of Science, through grant DE-SC0020170. K.A. was supported in part by the Natural Sciences and Engineering Research Council of Canada (NSERC) Postdoctoral Fellowship (PDF) program [application number PDF – 557232 – 2021]. We thank everyone who helped in any way or contributed valuable

discussions: Jennifer A. Lewis, Chris H. Rycroft, David A. Weitz, Dylan Barber, Bok Yeop Ahn, Simone Dussi, Meisam Bahari, Andrew Wong, Will Wang and Eric M. Fell.

References

1 M.-A. Goulet, M. Eikerling and E. Kjeang, Direct measurement of electrochemical reaction kinetics in flow-through porous electrodes, *Electrochem. Commun.*, 2015, **57**, 14–17.

2 K. V. Greco, A. Forner-Cuenca, A. Mularczyk, J. Eller and F. R. Brushett, Elucidating the nuanced effects of thermal pretreatment on carbon paper electrodes for vanadium redox flow batteries, *ACS Appl. Mater. Interfaces*, 2018, **10**(51), 44430–44442.

3 H. Park, G. Kwon, H. Lee, K. Lee, S. Y. Park and J. E. Kwon, *et al.*, In operando visualization of redox flow battery in membrane-free microfluidic platform, *Proc. Natl. Acad. Sci. U. S. A.*, 2022, **119**(9), e2114947119.

4 X. Huang, Q. Wang, X. Y. Chen and Z. J. Zhang, The effects of amine/nitro/hydroxyl groups on the benzene rings of redox additives on the electrochemical performance of carbon-based supercapacitors, *Phys. Chem. Chem. Phys.*, 2016, **18**(15), 10438–10452.

5 A. J. Slate, D. A. Brownson, A. S. A. Dena, G. C. Smith, K. A. Whitehead and C. E. Banks, Exploring the electrochemical performance of graphite and graphene paste electrodes composed of varying lateral flake sizes, *Phys. Chem. Chem. Phys.*, 2018, **20**(30), 20010–20022.

6 X. Zhou, T. Zhao, Y. Zeng, L. An and L. Wei, A highly permeable and enhanced surface area carbon-cloth electrode for vanadium redox flow batteries, *J. Power Sources*, 2016, **329**, 247–254.

7 Y. A. Gandomi, D. Aaron, T. Zawodzinski and M. Mench, In situ potential distribution measurement and validated model for all-vanadium redox flow battery, *J. Electrochem. Soc.*, 2015, **163**(1), A5188.

8 Q. Chen, M. R. Gerhardt and M. J. Aziz, Dissection of the voltage losses of an acidic quinone redox flow battery, *J. Electrochem. Soc.*, 2017, **164**(6), A1126.

9 L. Tong, Q. Chen, A. A. Wong, R. Gómez-Bombarelli, A. Aspuru-Guzik, R. G. Gordon and M. J. Aziz, UV-Vis spectrophotometry of quinone flow battery electrolyte for in situ monitoring and improved electrochemical modeling of potential and quinhydrone formation, *Phys. Chem. Chem. Phys.*, 2017, **19**(47), 31684–31691.

10 E. W. Zhao, T. Liu, E. Jónsson, J. Lee, I. Temprano and R. B. Jethwa, *et al.*, In situ NMR metrology reveals reaction mechanisms in redox flow batteries, *Nature*, 2020, **579**(7798), 224–228.

11 Y. Jing, E. W. Zhao, M.-A. Goulet, M. Bahari, E. M. Fell and S. Jin, *et al.*, In situ electrochemical recomposition of decomposed redox-active species in aqueous organic flow batteries, *Nat. Chem.*, 2022, **14**(10), 1103–1109.

12 E. Zhao, E. Jónsson, R. Jethwa, D. Hey, D. Lyu, A. Brookfield, P. A. Klusener, D. Collison and C. P. Grey, Coupled In Situ NMR and EPR Studies Reveal the Electron Transfer Rate and Electrolyte Decomposition in Redox Flow Batteries, *J. Am. Chem. Soc.*, 2021, **143**(4), 1885–1895.

13 J. Chuankun, L. Qi, S. Cheng-Jun, Y. Fan, R. Yang and L. Yadong, *et al.*, In Situ X-ray Near-Edge Absorption Spectroscopy Investigation of the State of Charge of All-Vanadium Redox Flow Batteries, *ACS Appl. Mater. Interfaces*, 2014, **6**(20), 17920–17925.

14 R. Jervis, L. D. Brown, T. P. Neville, J. Millichamp, D. P. Finegan and T. M. Heenan, *et al.*, Design of a miniature flow cell for in situ X-ray imaging of redox flow batteries, *J. Phys. D: Appl. Phys.*, 2016, **49**(43), 434002.

15 L. Bouffier and T. Doneux, Coupling electrochemistry with in situ fluorescence (confocal) microscopy, *Curr. Opin. Electrochem.*, 2017, **6**(1), 31–37.

16 R. C. Engstrom, S. Ghaffari and H. Qu, Fluorescence imaging of electrode-solution interfacial processes, *Anal. Chem.*, 1992, **64**(21), 2525–2529.

17 W. J. Bowyer, J. Xie and R. C. Engstrom, Fluorescence imaging of the heterogeneous reduction of oxygen, *Anal. Chem.*, 1996, **68**(13), 2005–2009.

18 J. E. Vitt and R. C. Engstrom, Imaging of oxygen evolution and oxide formation using quinine fluorescence, *Anal. Chem.*, 1997, **69**(6), 1070–1076.

19 J. C. O'Brien, J. Shumaker-Parry and R. C. Engstrom, Microelectrode control of surface-bound enzymatic activity, *Anal. Chem.*, 1998, **70**(7), 1307–1311.

20 J. P. Guerrette, S. J. Percival and B. Zhang, Fluorescence coupling for direct imaging of electrocatalytic heterogeneity, *J. Am. Chem. Soc.*, 2013, **135**(2), 855–861.

21 N. C. Rudd, S. Cannan, E. Bitziou, I. Ciani, A. L. Whitworth and P. R. Unwin, Fluorescence confocal laser scanning microscopy as a probe of pH gradients in electrode reactions and surface activity, *Anal. Chem.*, 2005, **77**(19), 6205–6217.

22 C. Renault, K. Marchuk, H. S. Ahn, E. J. Titus, J. Kim, K. A. Willets and A. J. Bard, Observation of nanometer-sized electro-active defects in insulating layers by fluorescence microscopy and electrochemistry, *Anal. Chem.*, 2015, **87**(11), 5730–5737.

23 J. L. Shepherd, A. Kell, E. Chung, C. W. Sinclar, M. S. Workentin and D. Bizzotto, Selective reductive desorption of a SAM-coated gold electrode revealed using fluorescence microscopy, *J. Am. Chem. Soc.*, 2004, **126**(26), 8329–8335.

24 A. Musgrove, A. Kell and D. Bizzotto, Fluorescence imaging of the oxidative desorption of a BODIPY-alkyl-thiol monolayer coated Au bead, *Langmuir*, 2008, **24**(15), 7881–7888.

25 J. R. Casanova-Moreno and D. Bizzotto, What happens to the thiolates created by reductively desorbing SAMs? An in situ study using fluorescence microscopy and electrochemistry, *Langmuir*, 2013, **29**(6), 2065–2074.

26 A. Meunier, E. Triffaux, D. Bizzotto, C. Buess-Herman and T. Doneux, In Situ Fluorescence Microscopy Study of the Interfacial Inhomogeneity of DNA Mixed Self-Assembled Monolayers at Gold Electrodes, *ChemElectroChem*, 2015, **2**(3), 434–442.

27 Z. L. Yu, J. Casanova-Moreno, I. Guryanov, F. Maran and D. Bizzotto, Influence of surface structure on single or

mixed component self-assembled monolayers via in situ spectroelectrochemical fluorescence imaging of the complete stereographic triangle on a single crystal Au bead electrode, *J. Am. Chem. Soc.*, 2015, **137**(1), 276–288.
28 C. Amatore, S. Arbault, Y. Chen, C. Crozatier, F. Lemaître and Y. Verchier, Coupling of electrochemistry and fluorescence microscopy at indium tin oxide microelectrodes for the analysis of single exocytotic events, *Angew. Chem., Int. Ed.*, 2006, **45**(24), 4000–4003.
29 D. S. Chung and R. C. Alkire, Confocal microscopy for simultaneous imaging of Cu electrodeposit morphology and adsorbate fluorescence, *J. Electrochem. Soc.*, 1997, **144**(5), 1529.
30 S. Cannan, I. D. Macklam and P. R. Unwin, Three-dimensional imaging of proton gradients at microelectrode surfaces using confocal laser scanning microscopy, *Electrochem. Commun.*, 2002, **4**(11), 886–892.
31 M. Yang, C. Batchelor-McAuley, E. Kätelhön and R. G. Compton, Reaction layer imaging using fluorescence electrochemical microscopy, *Anal. Chem.*, 2017, **89**(12), 6870–6877.
32 A. J. Welch, A. Q. Fenwick, A. Bohme, H.-Y. Chen, I. Sullivan and X. Li, *et al.*, Operando local pH measurement within gas diffusion electrodes performing electrochemical carbon dioxide reduction, *J. Phys. Chem. C*, 2021, **125**(38), 20896–20904.
33 A. Böhme, J. C. Bui, A. Q. Fenwick, R. Bhide, C. N. Feltenberger and A. J. Welch, *et al.*, Direct observation of the local microenvironment in inhomogeneous CO_2 reduction gas diffusion electrodes via versatile pOH imaging, *Energy Environ. Sci.*, 2023, **16**(4), 1783–1795.
34 A. A. Wong, S. M. Rubinstein and M. J. Aziz, Direct visualization of electrochemical reactions and heterogeneous transport within porous electrodes in operando by fluorescence microscopy, *Cell Rep. Phys. Sci.*, 2021, **2**(4), 100388.
35 J. S. Newman and W. Tiedemann, Flow-through porous electrodes, *Adv. Electrochem. Electrochem. Eng.*, 1978, **11**(4), 353–438.
36 Y. Jing, E. M. Fell, M. Wu, S. Jin, Y. Ji and D. A. Pollack, *et al.*, Anthraquinone flow battery reactants with nonhydrolyzable water-solubilizing chains introduced via a generic cross-coupling method, *ACS Energy Lett.*, 2021, **7**(1), 226–235.
37 D. G. Kwabi, Y. Ji and M. J. Aziz, Electrolyte lifetime in aqueous organic redox flow batteries: a critical review, *Chem. Rev.*, 2020, **120**(14), 6467–6489.
38 P. Symons, Quinones for redox flow batteries. Current Opinion in, *Electrochemistry*, 2021, **29**, 100759.
39 B. Huskinson, M. P. Marshak, C. Suh, S. Er, M. R. Gerhardt and C. J. Galvin, *et al.*, A metal-free organic–inorganic aqueous flow battery, *Nature*, 2014, **505**(7482), 195–198.
40 M. Wu, M. Bahari, E. M. Fell, R. G. Gordon and M. J. Aziz, High-performance anthraquinone with potentially low cost for aqueous redox flow batteries, *J. Mater. Chem. A*, 2021, **9**(47), 26709–26716.
41 Z. Yang, L. Tong, D. P. Tabor, E. S. Beh, M. A. Goulet and D. De Porcellinis, *et al.*, Alkaline benzoquinone aqueous flow battery for large-scale storage of electrical energy. Advanced Energy, *Materials*, 2018, **8**(8), 1702056.
42 D. G. Kwabi, K. Lin, Y. Ji, E. F. Kerr, M.-A. Goulet and D. De Porcellinis, *et al.*, Alkaline quinone flow battery with long lifetime at pH 12, *Joule*, 2018, **2**(9), 1894–1906.
43 M. L. Perry, R. M. Darling and R. Zaffou, High power density redox flow battery cells, *ECS Trans.*, 2013, **53**(7), 7.
44 Q. Chen, L. Eisenach and M. J. Aziz, Cycling analysis of a quinone-bromide redox flow battery, *J. Electrochem. Soc.*, 2015, **163**(1), A5057.
45 M.-A. Goulet and M. J. Aziz, Flow battery molecular reactant stability determined by symmetric cell cycling methods, *J. Electrochem. Soc.*, 2018, **165**(7), A1466–A1477.
46 C. Wiberg, T. J. Carney, F. Brushett, E. Ahlberg and E. Wang, Dimerization of 9,10-anthraquinone-2,7-Disulfonic acid (AQDS), *Electrochim. Acta*, 2019, **317**, 478–485.
47 T. J. Carney, S. J. Collins, J. S. Moore and F. R. Brushett, Concentration-dependent dimerization of anthraquinone disulfonic acid and its impact on charge storage, *Chem. Mater.*, 2017, **29**(11), 4801–4810.

Quantitative Local State of Charge Mapping by *Operando* Electrochemical Fluorescence Microscopy in Porous Electrodes

Anton M. Graf[a,†], Thomas Cochard[a,†], Kiana Amini[a,b], Michael S. Emanuel[a], Shmuel M. Rubinstein*[,c] and Michael J. Aziz*[,a]

a. *Harvard John A. Paulson School of Engineering and Applied Sciences, 29 Oxford St., Cambridge, MA02138, USA.*

b. Present address: Department of Materials Engineering, University of British Columbia, Vancouver, BC Canada V6T 1Z4

c. Racah Institute of Physics, The Hebrew University of Jerusalem, Jerusalem, Israel.

† These authors contributed equally to this work.

Electronic Supporting Information (ESI)

ESI 1: Electrochemical setup and electrolyte preparation

Fabrication of the electrochemical cell: The electrochemical cell was constructed by assembling two acrylic plates, which sandwiched two Polydimethylsiloxane (PDMS) half-cells separated by a Nafion 212 membrane, as illustrated in Figure S1(A). The PDMS components were fabricated through 3D printing and molding. Initially, a mold design was created, and 3D printed using Stereolithography (Form 3, Formlabs). Subsequently, PDMS was poured into each mold and subjected to vacuum treatment to eliminate any air bubbles that could compromise transparency and proper sealing of the components. The PDMS parts were then cured overnight at 65°C. Figure S1(B) showcases the transparency achieved with the PDMS 3D printed mold. To assemble the PDMS half-cells, electrodes, and membrane, transparent acrylic endplates and screws were used to compress the components.

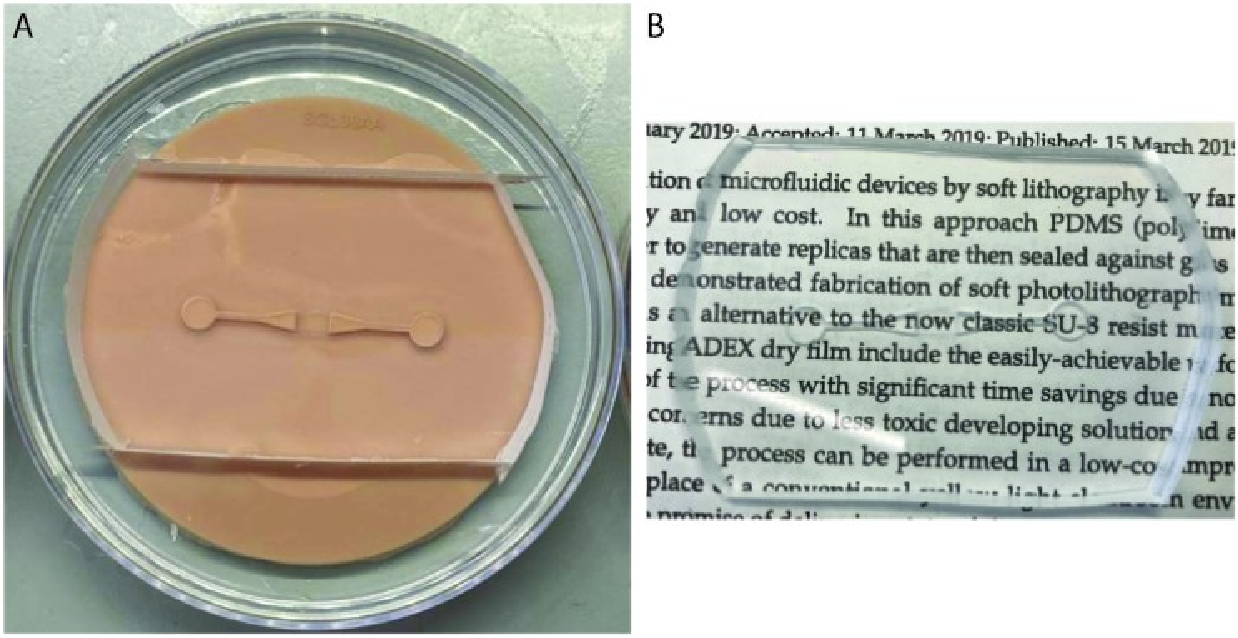

Figure S1: PDMS molding process. (A**)** 3D printed mold for the AQDS side with the flow channel feature in the center (orange disk) in a petri-dish where the PDMS is poured. (B**)** AQDS side half-cell removed from the mold after curing. The transparency of the pieces obtained is showcased by the text which is clearly readable.

Electrolyte: For the electrolyte concentration series, a 40 mM stock solution was prepared by dissolving 2,7 anthraquinone disulfonate (AQDS) salt in 1M sulfuric acid. AQDS with a purity of 98% was procured from BocSciences. Electrolyte solutions of 40, 30, 20, and 10 mM were obtained by diluting the stock solution with 1M sulfuric acid. To eliminate oxygen from the electrolyte, each solution was purged with nitrogen (N2, ultra-high purity, Airgas) for 30 minutes prior to each experiment. The electrochemical cell itself was also purged with nitrogen for 30 minutes, bringing the system to operating pressures to ensure the absence of leaks and remove any remaining oxygen. In all experiments detailed in this report, the electrolyte was continuously pumped through the cell at a constant flow rate of 2 mm/sec using a Harvard syringe pump. Further information can be found in the main text.

Electrochemical experiments:

AvCarb MGL 190 carbon paper of nominal thickness 190 µm was used as the working electrode. The electrode was baked for 24 h at 400 °C prior to the experiment. On the counter electrode side, a 0.5 mg/cm² 60% Platinum on Vulcan - Carbon Paper Electrode from FuelCellStore was used to oxidize hydrogen gas. Nafion 212, used as membrane, was soaked in 1 M sulfuric acid prior to the experiments.

For the electrochemical experiments, a portable Gamry Instruments Reference 3000 potentiostat/galvanostat/ZRA was employed. The electrochemical reaction was induced using a multi-step chronoamperometry protocol. Initially, the open circuit potential (OCV) was determined for the two-electrode configuration of the hybrid cell. Subsequently, incremental potential steps were applied and maintained at a constant value for 60 seconds each. In between each potential step, the cell was purged at OCV conditions for 30 seconds. A sampling rate of 0.5 seconds was employed.

ESI 2: *In situ* confocal microscopy

Fluorescence microscopy was conducted using a spinning disk microscope while the electrochemical flow cell was in operation. The setup consisted of a Leica MDi8 microscope body and an Andor CSU-W spinning disk system. A Leica 10x/0.3NA HC PL FLUOTAR lens was employed for imaging.

For all experiments presented in this study, the following parameters were utilized: a pinhole size of 50 µm, an exposure time of 2 seconds, and an acquisition time of 2.5 seconds per frame.

Excitation light at a wavelength of 405 nm was provided by a laser, and emission light was filtered through a green bandpass filter (approximately 475-525 nm). The laser intensity was set to 50% of its maximum capacity. No gain or offset was applied. The laser was consistently on with the exposure time mentioned above. The intensity and exposure time are crucial for controlling image brightness. These parameters were adjusted to optimize the number of discrete intensity values across the grayscale (each image was captured at 16-bit depth, corresponding to 65,536 gray levels), ensuring optimal brightness.

ESI 3: *Ex-situ* photophysical characterization

The photophysical experiments involving emission and absorption scans were conducted using a BioTek Synergy HT plate reader equipped with a 405 nm excitation source and an emission scan capability. In each well of a GREINER MICROPLATE (96 WELL, PS, F-BOTTOM, μCLEAR®, BLACK, MED. BINDING), 200 μL of each sample was loaded.

We prepared the 40 mM AQDS solutions following the procedure outlined in ESI 1. These solutions were then transferred to a glovebox and subjected to charging versus V3+/V4+ under a nitrogen (N2) atmosphere inside a bench-scale flow battery. The 40 mM solution was charged to SOCs of 0%, 30%, 40%, 60%, 70%, 80%, and 90% and results are shown in the main text. For the ex-situ tests, flow battery experiments utilized cell components sourced from Fuel Cell Technologies Inc. (Albuquerque, NM). Each half-cell of the battery was equipped with interdigitated flow fields made from pyro-sealed POCO graphite flow plates, with 3 layers of carbon paper (SGL 39AA) per side, baked at 400 °C overnight. During cell assembly, the applied torque was 60 lb-in (6.78 N·m) across eight 3/8”–24 bolts, resulting in a load of approximately 800 lbs per bolt. The geometric area of each electrode was 5 cm². A Nafion 212 cation exchange membrane and a 10 mil Viton gasket separated the two half-cells. The cells were operated inside a nitrogen-filled glovebox. To ensure accuracy, each solution underwent two battery cycles, resulting in a consistent charge efficiency of 98% for all solutions, thereby minimizing systematic errors. To prevent reoxidation due to the diffusion of atmospheric oxygen into the electrolytes, the electrolyte solutions were transferred to a well plate inside the glovebox and sealed with a lid.

ESI 4: 1:1 (AQDS:H_2AQDS) binding dimer model

The quinhydrone concentration at each SOC value can be calculated from a system of equations. Using the equilibrium constant of dimer formation of $K_{dim} = 80\ M^{-1}$ from the literature(1) and the total concentration of the reactants participating in the electrochemical reaction, which is equal to the initial concentration of AQDS in each experiment, a parametric curve for each species concentration as a function of SOC can be computed. The system of equations is shown below:

$$K_{dim} = 80\ M^{-1} = \frac{[QH]}{[AQDS][H_2AQDS]} \tag{S4.1}$$

$$[AQDS]_0 = [AQDS] + [H_2AQDS] + 2[QH] \tag{S4.2}$$

$$SOC = \frac{[H_2AQDS] + [QH]}{[AQDS] + [H_2AQDS] + 2[QH]} \tag{S4.3}$$

The system of equations is solved for different $[AQDS]_0$.

For the reactant concentrations used in this study the plots in Figure S2 were obtained.

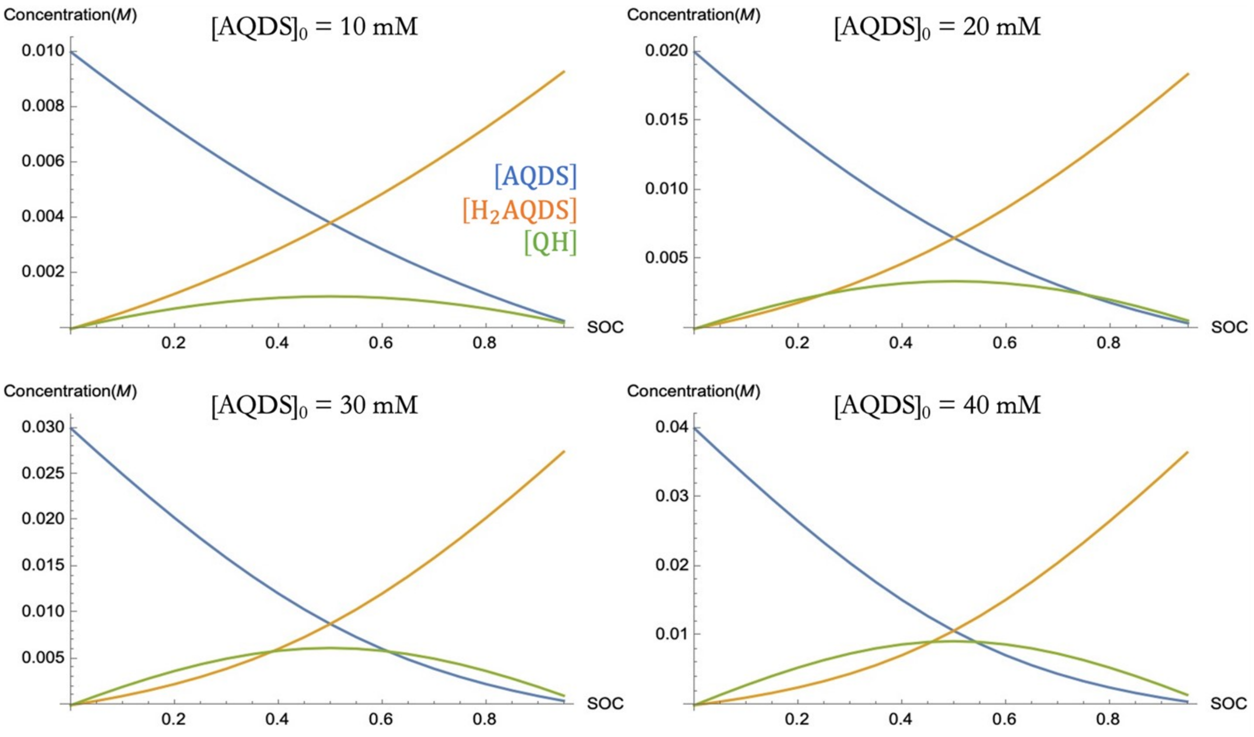

Figure S2: 1:1 (AQDS:H_2AQDS) binding dimer model. Prediction of the theoretical concentration profiles for AQDS, H_2AQDS, and the QH as a function of SOC, calculated using the dimer model. The simulations are performed at fixed $[AQDS]_0$ of 10, 20, 30, and 40 mM and K_{dim} = 80 M^{-1}.

With increasing $[AQDS]_0$, it is evident that the proportion of dimer to the total concentration grows in the presented cases, and the concentrations of individual molecular species exhibit increasingly nonlinear variations with respect to the SOC. Consequently, it is essential to account for the influence of dimer formation on fluorescence intensity, particularly at high concentrations, in order to accurately quantify the SOC. The plate reader data in Figure 2(C) demonstrate that the intensity of the 40 mM solution follows the same nonlinear trend as the H_2AQDS concentration.

ESI 5: Theoretical background of concentration fields in flow devices

In electrochemical flow devices, the temporal change of the concentration fields can be modeled by the sum of mass-transport and electrochemical source terms, namely advection A_j, diffusion D_j, electromigration ε_j and the (Butler-Volmer) source term S.

$$\frac{\partial C_j}{\partial t} = A_j + D_j + \varepsilon_j + S \tag{S5.1}$$

A_j describes the net flow through the electrode and is given by a function of the geometry u and the gradient of the concentration of interest ∇C_j,

$$A_j = -u \cdot \nabla C_j \tag{S5.2}$$

D_j as derived by Fick's law can be calculated from the diffusion coefficient of the molecular species d_j and the Laplacian of the concentration of interest $\nabla^2 C_j$,

$$D_j = d_j \cdot \nabla^2 C_j \tag{S5.3}$$

ε_j describes the bias of charged entities through the electric field and is given by the charge z_j, Faraday's constant F, the gas constant R, the temperature T, and the electric field $-\nabla \phi_L$,

$$\varepsilon_j = \frac{z_j \cdot D_j \cdot F}{R \cdot T} \cdot \nabla \cdot (C_j \cdot \nabla\phi_L) \tag{S5.4}$$

Adding all terms together we obtain the following partial differential Eq. A.1 for the temporal change of the concentration as a function of current, potential and mass-transport:

$$\frac{\partial C_j}{\partial t} = -u \cdot \nabla C_j + d_j \cdot \nabla^2 C_j + \frac{z_j D_j F}{R \cdot T} \cdot \nabla \cdot \left(C_j \cdot \nabla\phi_L\right) + S_j \tag{S5.5}$$

The connection between the applied potential and the current is given through the electrochemical source term (Butler-Volmer equation) measuring the overall rate of the redox reaction of AQDS. The source term can be computed given the overpotential (η), the geometric area of the electrode interface (a), the reaction rate constant (k), the charge transfer coefficients of the respective redox-state (α_i) as well as the concentration of the reactant in each redox-state (C_i).

$$S = a \cdot k \cdot C_A^{\alpha_A} \cdot C_B^{\alpha_B} \cdot \left[\exp\left(\frac{n_e \cdot F \cdot \alpha_A}{R \cdot T} \cdot \eta\right) - \exp\left(\frac{n_e \cdot F \cdot \alpha_B}{R \cdot T} \cdot \eta\right)\right] \tag{S5.6}$$

The applied overpotentials cause the current response which is monitored over the duration of the experiment. Consequently, current and overpotential as well as fluorescence intensity and concentration can be directly related. Both pairs of physical parameters must be connected to finally interpret the fluorescence data and derive conclusions about current, potential and flow.

ESI 6: Data calibration and SOC mapping

As part of our calibration procedure, we considered the fluorescence contributions of each molecular species involved, i.e. AQDS, H_2AQDS and QH, which are required for proper quantification of the local SOC. The various contributions are displayed schematically in Figure S3.

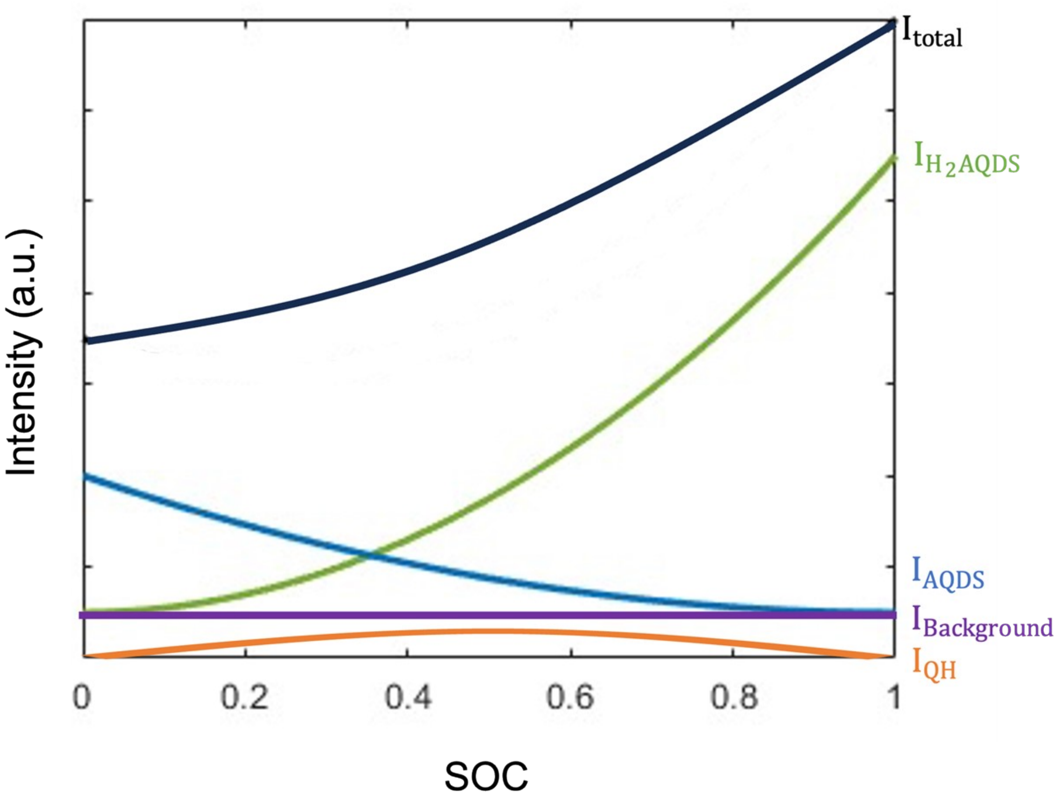

Figure S3: Schematic depiction (not to scale) of different contributions to the spatially averaged raw intensity I_{total}. For the calibration of the intensity maps to obtain SOC maps we need to distinguish between the different species contributing to I_{total}. The black solid line schematically shows I_{total}that is obtained in experiment. $I_{Background}$ is the background signal which remains constant in every image. I_{QH} corresponds to the dimer intensity which is expected to have small contribution to I_{tot} but is estimated independently. I_{AQDS} is the native fluorescence of AQDS and I_{H_2AQDS} is the fluorescence of H_2AQDS which has the highest contribution to I_{total}.

Our experimental data for the SOC estimation comprised 29 images. A single *ex situ* image taken at a high and homogeneous (but unknown) H_2AQDS concentration; and 28 images taken for varying applied overpotentials with 4 total AQDS concentrations crossed with 7 applied voltages. As the analysis is done at the individual pixel level, it is critical for the images to be aligned on that scale based on the *ex-situ* image. This was done using the CV2 computer vision library and resulted in a mean shift of 1.8 pixels. Once all the images were aligned, we assigned pixels into three categories: excessively dim; excessively bright; and reliable pixels to be included in the analysis. We hypothesize that excessively dim pixels were due to obstructing fibers, and excessively bright pixels were caused by highly reflective heterophase impurities. We set thresholds for dim and bright pixels at quantiles 0.55 and 0.995, respectively. These thresholds were set by a combination of a qualitative visual review of the data with a Gaussian mixture model to set the lower threshold. As the location of the fibers remains fixed in every image, a pixel I_{ri} on one of the reaction images was considered valid when the corresponding pixel B_i was valid on the *ex-situ* image, and the pixel fell within the specified quantiles of intensity for that reaction. The remaining pixels, corresponding to fibers and other heterophase impurities, were set to be NaN and were not further considered in our analysis, as demonstrated for the example in Figure S4.

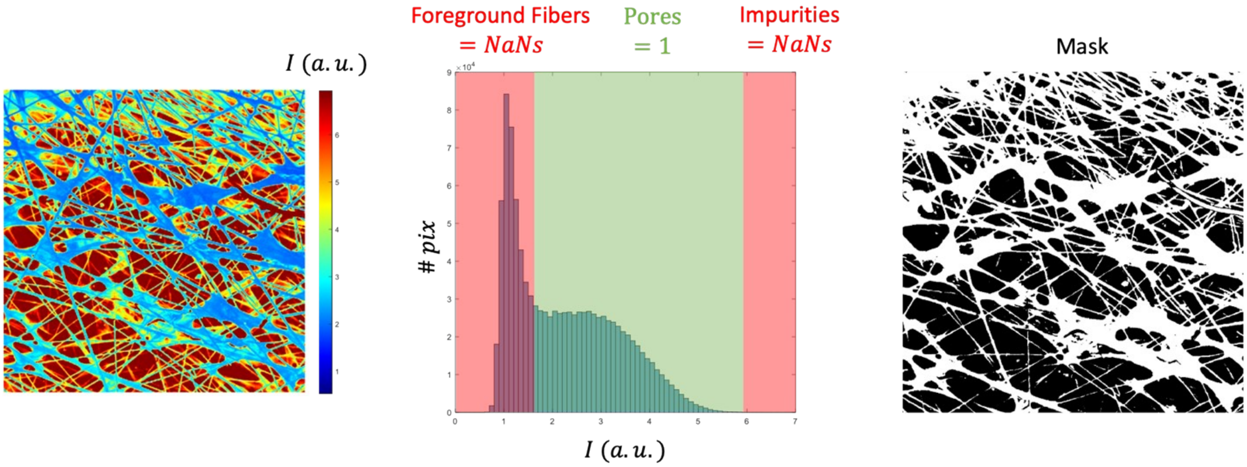

Figure S4: Selection of valid pixels for SOC maps. (Left) shows the raw intensity image in arbitrary units. (Middle) the histogram of the image is shown with schematic of the manually selected low and high intensity cutoffs. The red areas correspond to the pixels that were set to NaN values and are identified as fibers or impurities. The green area corresponds to the "good" pixels in the pores filled with electrolyte that are considered for further image processing. (Right) shows a visualization of the mask image that contains all valid pixels (in black) and NaN pixels in white.

This data filtering reduced the size of our calibration set from 29.4 million to 11.7 million pixels. The result of the image data processing was an array of *ex situ* intensities B_i and arrays I_r for each reaction condition.

We also had 28 utilizations u_r corresponding to each reaction and calculated by Eq. 3.2. We posit a linear relationship between the electrochemical utilization u_r and the mean state of charge $\bar{S}_r$. When the system is not mass transport limited, the mean field theory should be a highly accurate approximation *on average* over a mesoscale patch of space, even if it does not hold uniformly over very small areas. Most of our reactions had utilizations below 50%, justifying the claim that mass transport limitations were not binding and the use of this approximation. In the simple mean field theory without mass transport limitations, the solution is a smooth constant gradient in the state of charge between 0 at the inlet and u at the outlet. The mean state of charge $\bar{S}$ and utilization u are thus related by $\bar{S} = u x_m / L$ where x_m is the position of the midpoint of the image and L is the length of the electrode. In our study, the ratio x_m / L = 0.63.

There are three electroactive species in this study, namely the oxidized state AQDS; the reduced state H_2AQDS; and the dimer QH. The concentrations of these species are subject to two constraints,

$$[AQDS] + [H_2AQDS] + 2\,[QH] = [AQDS]_0 \quad \text{(S6.1a)}$$

$$[QH] = K\,[AQDS]\,[H_2AQDS] \quad \text{(S6.1b)}$$

Eq. S6.1a is conservation of the anthraquninone species in their various forms, and Eq. S6.1b is the chemical equilibrium governing dimer formation. It is straightforward to solve Eq. S6.1 for the concentration of all three species using the relative concentration Y of the reduced species defined in Eq. 3.5. The solutions are:

$$[AQDS] = \frac{1 - Y}{1 + 2\,R\,Y} \cdot [AQDS]_0 \quad \text{(S6.2a)}$$

$$[H_2AQDS] = Y \cdot [AQDS]_0 \quad \text{(S6.2b)}$$

$$[QH] = \frac{RY}{1 + 2\,R\,Y}\,[AQDS]_0 \quad \text{(S6.2c)}$$

where R = $K\,[AQDS]_0$ is the dimensionless rate constant for the dimer formation is.

We next made an initial estimate of the brightness coefficients α, β, γ, δ. To formulate this estimate, we made the preliminary assumption (later relaxed in the final estimation) that the concentrations of the electroactive species were uniform for each reaction. Using Eq. S6.2, we constructed a numerical table mapping an input reduced fraction Y to an output state of charge. There is one table for each initial concentration $[AQDS]_0$. These tables were all monotonically increasing as we expected, and we used the data points to construct four numerical functions mapping between SOC and Y at the various $[AQDS]_0$. We converted the utilizations u_r to a mean SOC $\bar{S}_r$ for each reaction; interpolated $\bar{S}_r$ to obtain $\bar{Y}_r$; and then solved for the equation of each species using Eq. S6.2. We completed this step by solving a linear least squares problem of the form **I** = **XC**. The left-hand side was the mean image intensity for the 28 reactions. The design matrix **X** has 28 rows and four columns [AQDS], [H_2AQDS], [QH], 1. The estimated coefficients are **C** = [α, β, γ, δ]. This regression achieved an excellent fit with an R squared value of 0.9632.

The estimated coefficients included a large, positive value for β (the brightness of H_2AQDS) and much smaller values for AQDS and QH, as expected.

Once the brightness coefficients were available, we built a table with the predicted light production P as a function of Y by Eq. 3.3. This led to a monotonic function that was interpolated to produce a mapping function Y(P). We finally estimated the state of charge by applying Eq. 3.4 once we have the optical factor F_i at each pixel. We obtained the optical factor by applying the assumption that the bright *ex situ* image is homogeneous, yielding the direct calculation $F_i = B_i/\bar{B}$, where $\bar{B}$ is the mean intensity on the ex-situ image. The resulting estimates of the state of charge are visually plausible and have an excellent fit to the experimental brightness.

At this stage we made a further refinement of the model. We relinquished the assumption used to estimate the brightness coefficients that the concentration was uniform on each reaction image. We also insisted that the model recover the assumed mean state of charge on each reaction; the initial estimate was close but had an RMS error of 0.031. This model was estimated by an iterative application of three computational steps until convergence was achieved. These steps are: (1) refine the estimate of the optical factor; (2) refine the estimate of the brightness coefficients; (3) shift the estimated concentrations to match the mean state of charge $\bar{S}_r$.

The concentration shifts are performed after applying a logit transform of the estimated Y for each reaction. At each step, logit(Y) is shifted by one step of Newton's method using a numerical derivative. Four steps of Newton's method are sufficient to match $\bar{S}_r$ to six decimal places. The update to the brightness coefficients is analogous to the initial estimate. This time, however, instead of a least squares problem with 28 rows (one per reaction), there are 11.7 million rows (one per valid pixel). The left-hand side of the least squares equation is the observed intensity, and the design matrix X is as before, but each row is now scaled by the optical factor. We can succinctly write the design matrix entries as

$X_{ri} = \left[[AQDS], [H_2AQDS], [QH], 1\right] \cdot F_i$ This regression **I** = **X C** provides both an updated estimate of the brightness coefficients and a standard error σ_I on the recovered brightness.

The update to the optical factors F is new to this stage of the estimation. If we consider pixel *i* in isolation, Eq. 3.4 implies that we can construct a linear regression $\mathbf{I_r} = \mathbf{P_r}$ F, where $\mathbf{I_r}$ and $\mathbf{P_r}$ are both column vectors with 28 rows, and F is the optical factor to be estimated. This regression can be augmented to include an additional 29th row from the *ex situ* image with left and right sides B_i and $\bar{B}$, respectively. This regression also provides a standard error σ_F on the optical factor.

This model was initialized with preliminary estimates for the brightness coefficients and optical factors described above. It was then iterated for nine steps until convergence criteria for small changes in parameter values were met. The converged model includes estimates for the concentration of all three species, from which we can easily compute the estimated SOC. The model also estimates standard errors in I and F. We then compute a total standard error by assuming that the errors in I and F are independent. The result of this calculation is an RMS error of 0.00526 SOC units over all 28 reactions. The attribution of the error is 0.00422 due to uncertainty in I and 0.00314 due to uncertainty in F. It is important to acknowledge that even after the calibration procedure, certain residual background fibers and pore depth effects persisted, which have the potential to introduce minor systematic errors.

Comparison with a constant SOC gradient assumption:

We assumed that over large scales, as the 1.2x1.2 mm imaging frame, a simplified assumption of a constant SOC gradient along x and uniform along y can be used to estimate $\bar{S}$. The results are then given by $\bar{S} = ux_m/L$ as demonstrated in Figure S5.

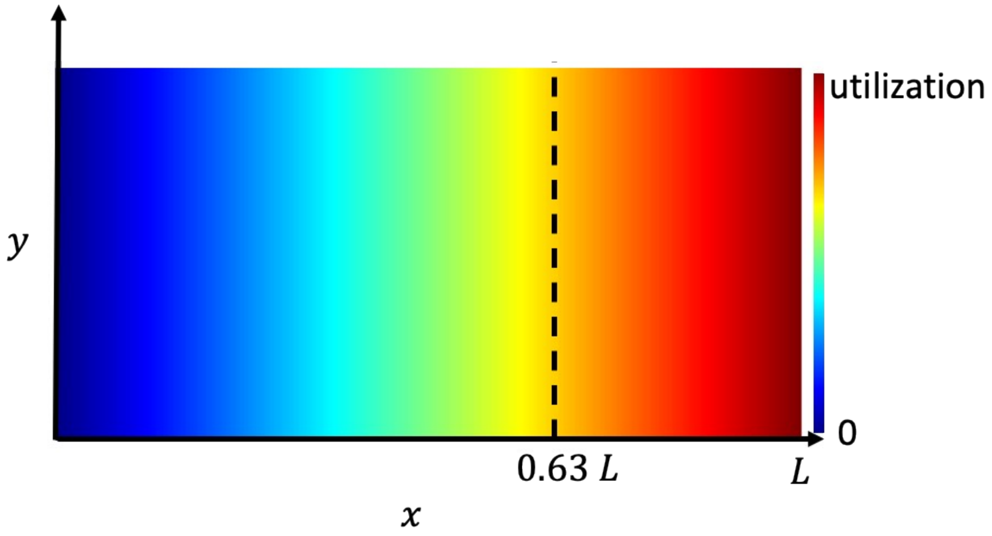

Figure S5: Schematic of simple constant gradient assumption. The rectangle corresponds to the working electrode where the fully oxidized electrolyte enters on the left side and gets reduced in the form of a constant gradient along x towards the outlet.

The color map indicates the utilization of 0% in blue and the maximum utilization, at the end of the electrode, in red. In our study, the image is centered at $x_m/L =$ 0.63.

For a comparison of our results with the simple assumption of a smooth, constant gradient, we generated simulated SOC maps at two distinct utilizations (0.3 and 0.6), maintaining x_m consistent with the experimental location of the imaging center at 0.63L, as depicted in Figure S6. A mask was superimposed on the images, designating pixels in regions obscured by fibers as NaNs. Notably, the histograms indicate that the distributions largely resemble rectangular shapes, even after the exclusion of the masked pixels.

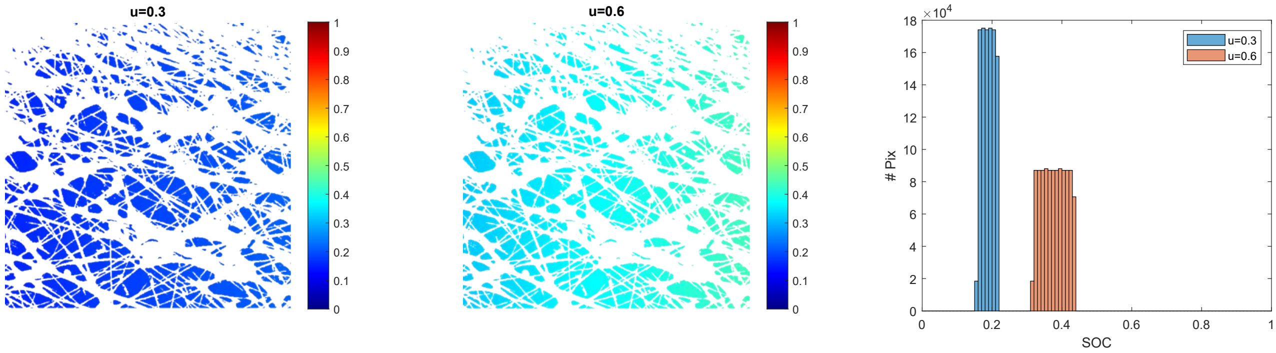

Figure S6: Spatial mapping of the simplified model featuring a constant gradient, tailored to the specific imaging frame and incorporating the position and mask derived from the actual experiment. On the left, a simulated 2D SOC corresponds to an electrolyte utilization of 0.3, while the central image represents a utilization of 0.6. The rightmost image presents the associated histograms, which largely maintain rectangular distributions even in the presence of NaN values.

References

1. Tong L, Chen Q, Wong AA, Gómez-Bombarelli R, Aspuru-Guzik A, Gordon RG, Aziz MJ. UV-Vis spectrophotometry of quinone flow battery electrolyte for in situ monitoring and improved electrochemical modeling of potential and quinhydrone formation. Physical Chemistry Chemical Physics. 2017;19(47):31684-91.